Supplementary Information

for

Mapping of dynamic allostery within p38 alpha kinase via network analyses and NMR spectroscopy

Suchandra Roy Acharyya, Jörn Weisner, Rafael C. Bernardi, and Rasmus Linser

Table of contents- Figures

Table of contents- Tables

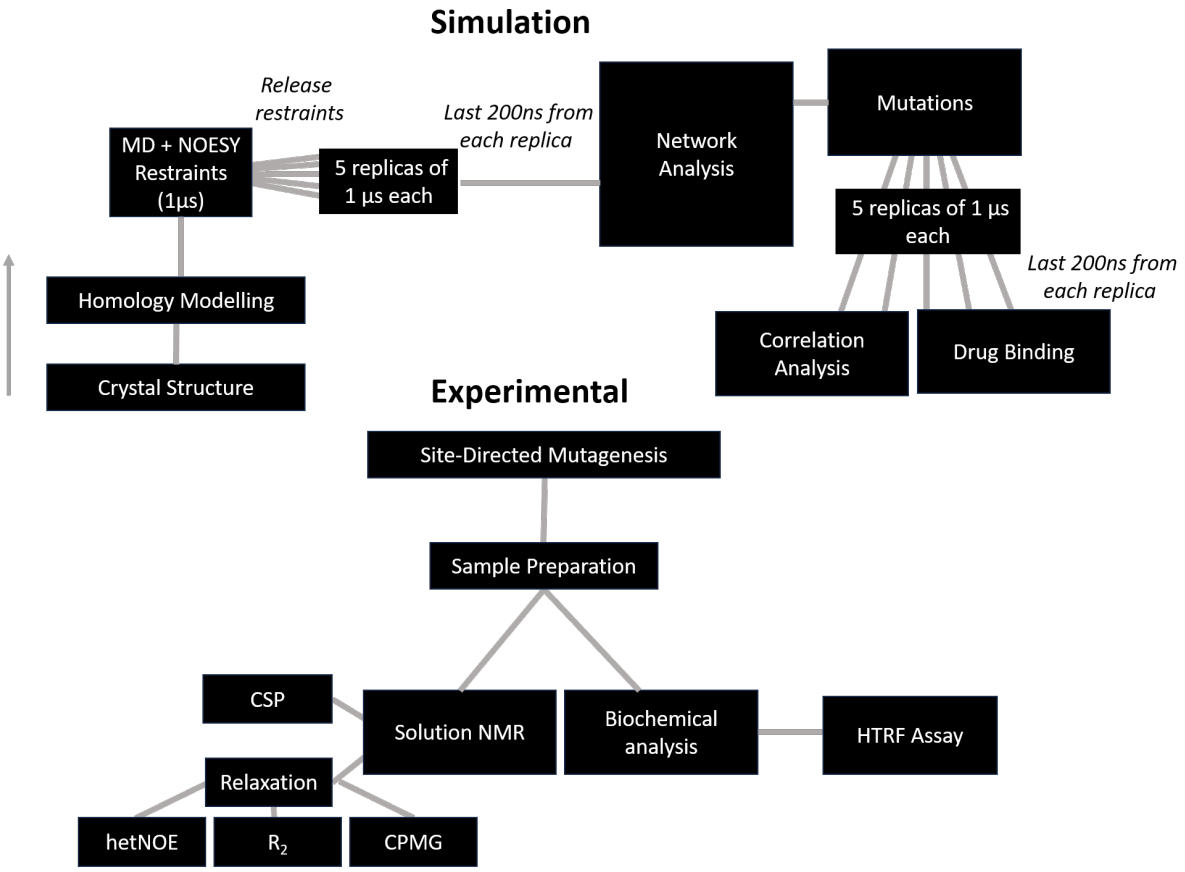

Fig. S1: Schematic representation of the methodology to identify the communicators and validate them experimentally and computationally.

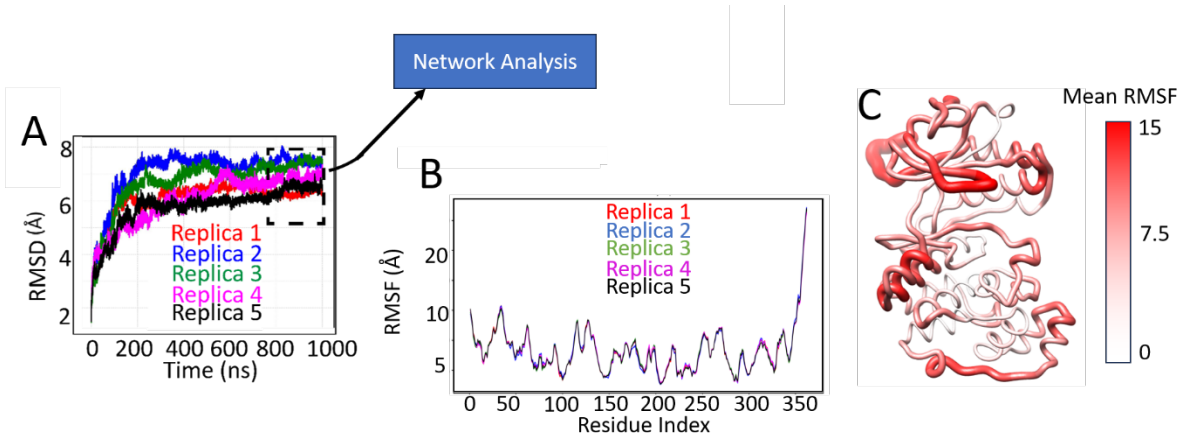

Fig. S2: A) Backbone RMSD of the apoprotein across five independent 1 µs replicas; the final 200 ns of each replica were used for network analysis. **B**) Overlay of RMSD traces for all five apoprotein replicas, highlighting convergence. **C**) Average per-residue RMSF mapped onto the protein structure to visualize flexibility.

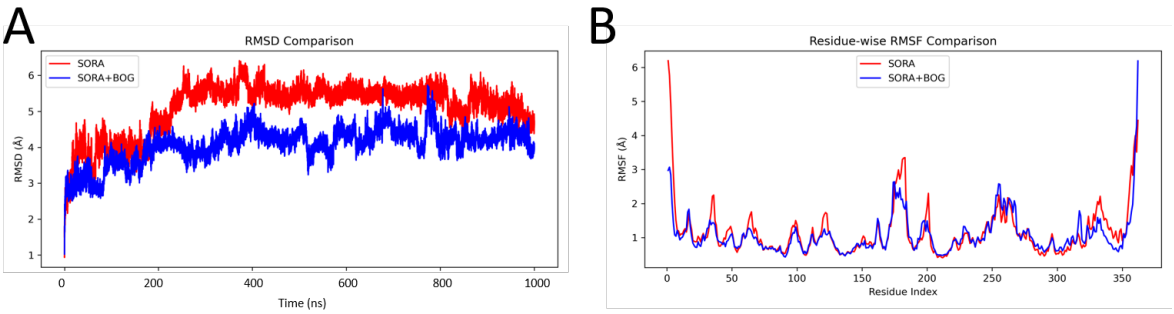

Fig. S3: A) RMSD of the simulations using starting crystal structures 3HEG (p38a bound to sorafenib only; red) and 3GCS (Sora + BOG; blue) **B**) RMSF of the simulations using starting crystal structures 3HEG (Sorafenib with p38α; red) and 3GCS (Sora + BOG with p38α ; blue).

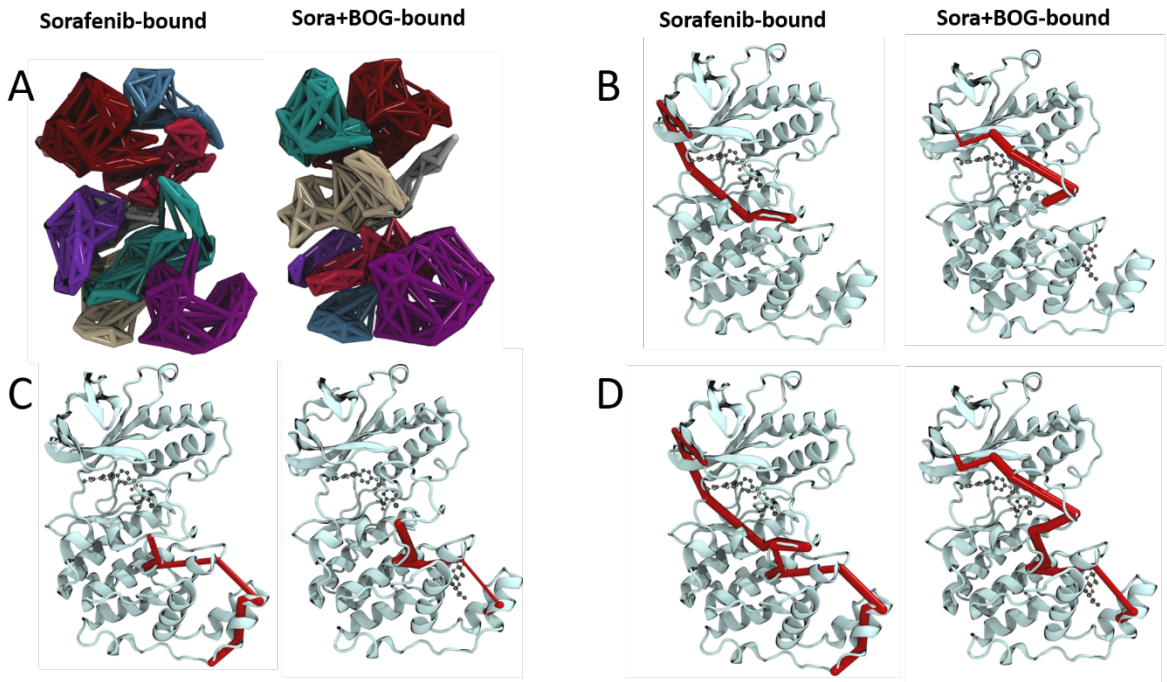

Fig. S4: Dynamical network analysis of MD trajectories starting with the crystal structures. A) Differences in communities when BOG binds to the lipid pocket. **B**) Differences in pathways upon BOG binding from the allosteric pocket to the activation loop. **C**) Differences in pathways upon BOG binding from the lipid pocket to the activation loop. **D**) Differences in pathways upon BOG binding from the lipid pocket directly to the allosteric pocket.

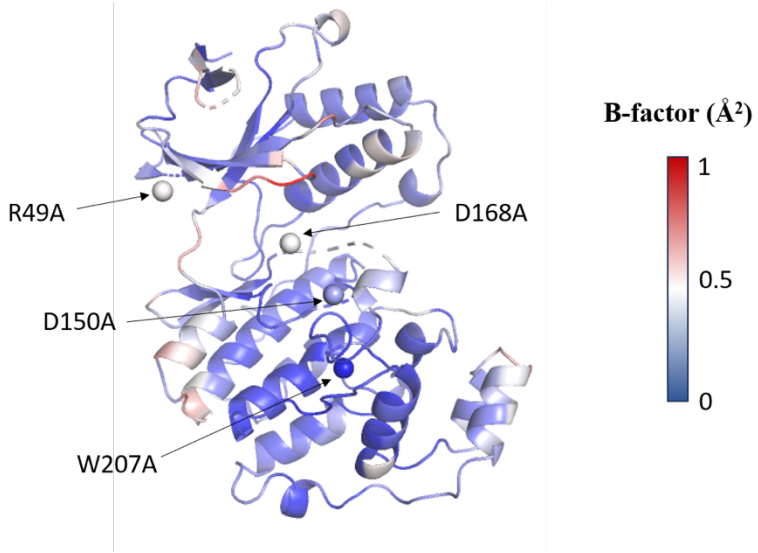

Fig. S5: B-factors of X-ray crystal structure along the protein. Temperature B-factors (Debye-Waller factors) are shown for the crystal structure PDB 3HEG.

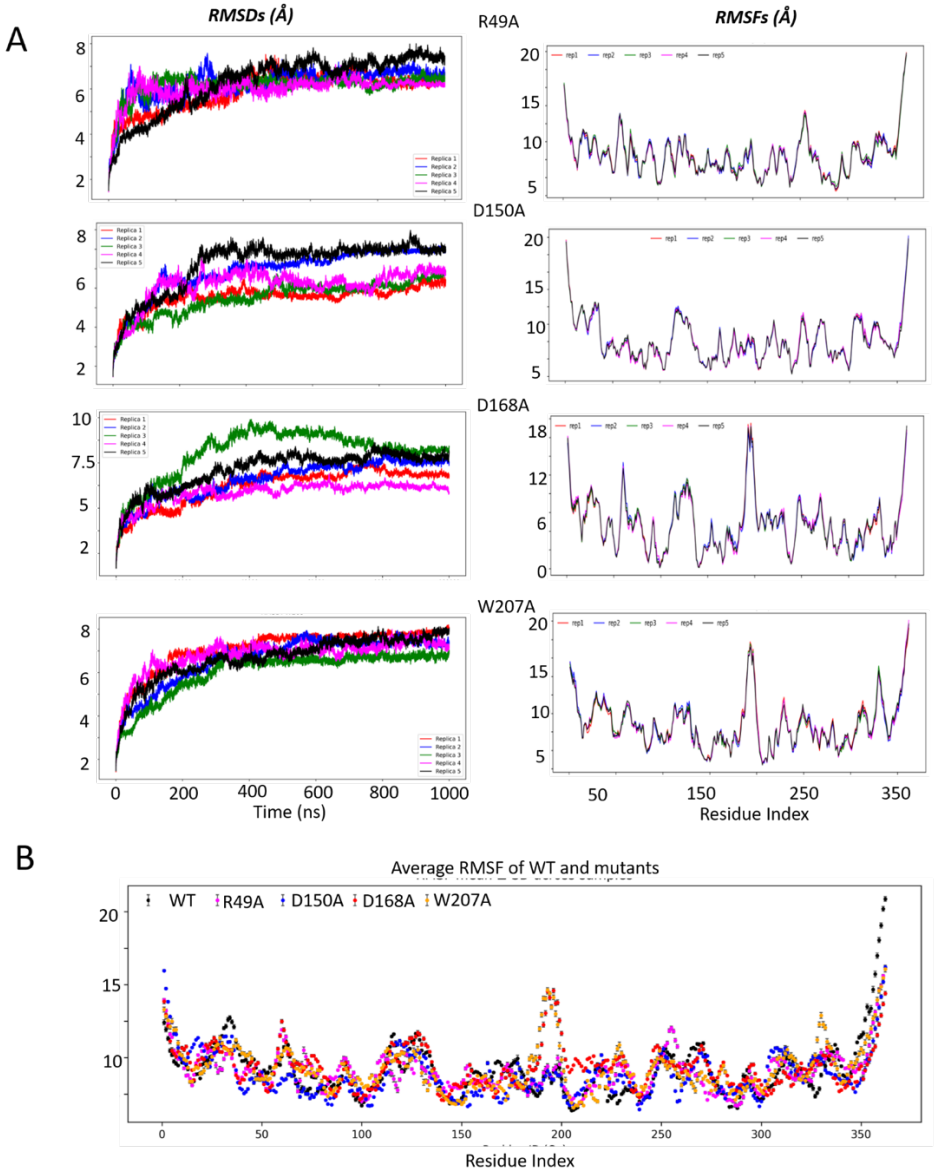

Fig. S6: A) RMSDs and RMSFs of five replicas per mutant. The last 200 ns were used for network and correlation analysis. **B)** Mean and SD of all the RMSFs compared with the wildtype.

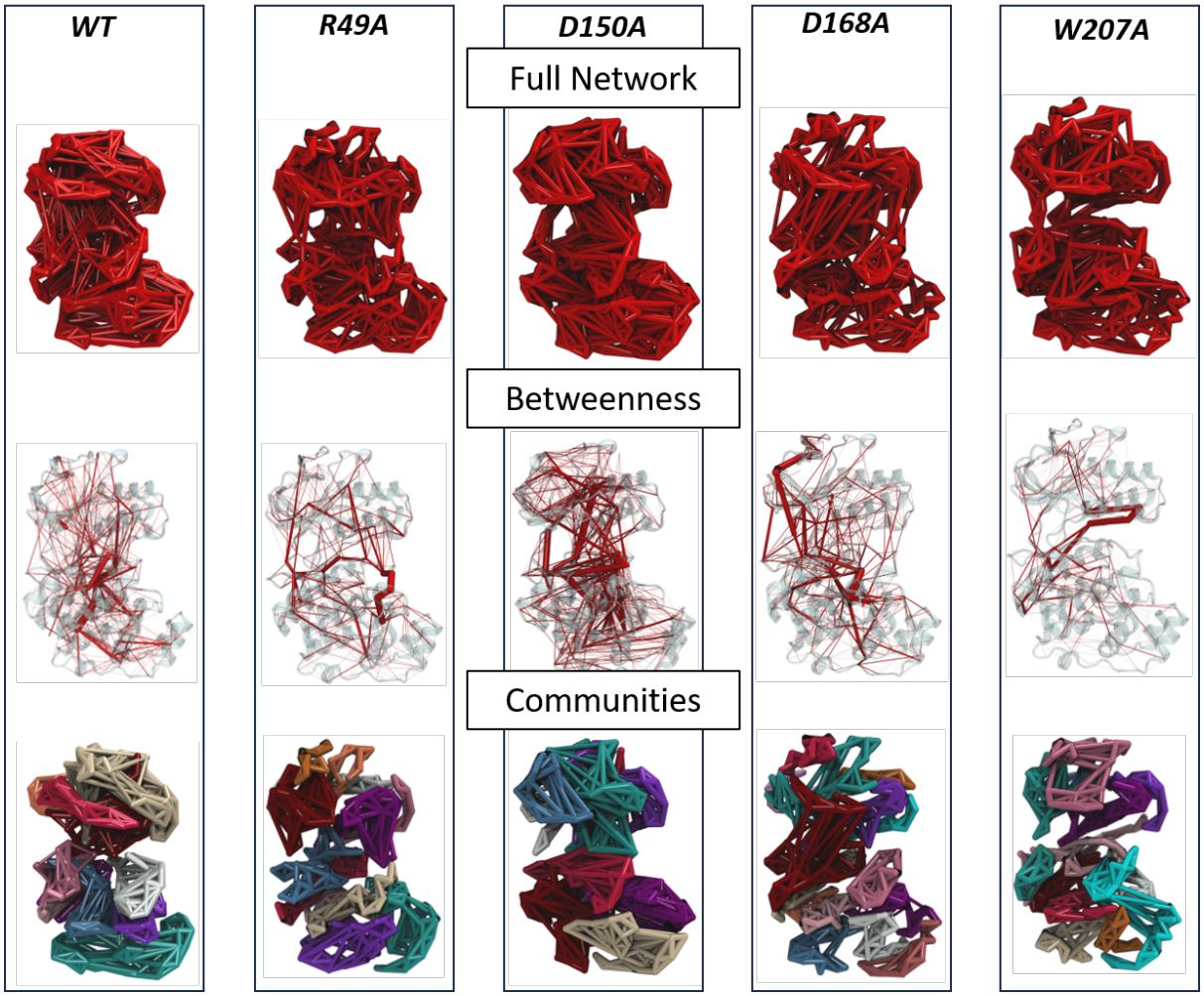

Fig. S7: Network analysis by Dynetan, mainly betweenness and communities of the mutants. The top shows the entire network, while the center depicts betweenness, and the bottom shows the clusters found in each of the mutants.

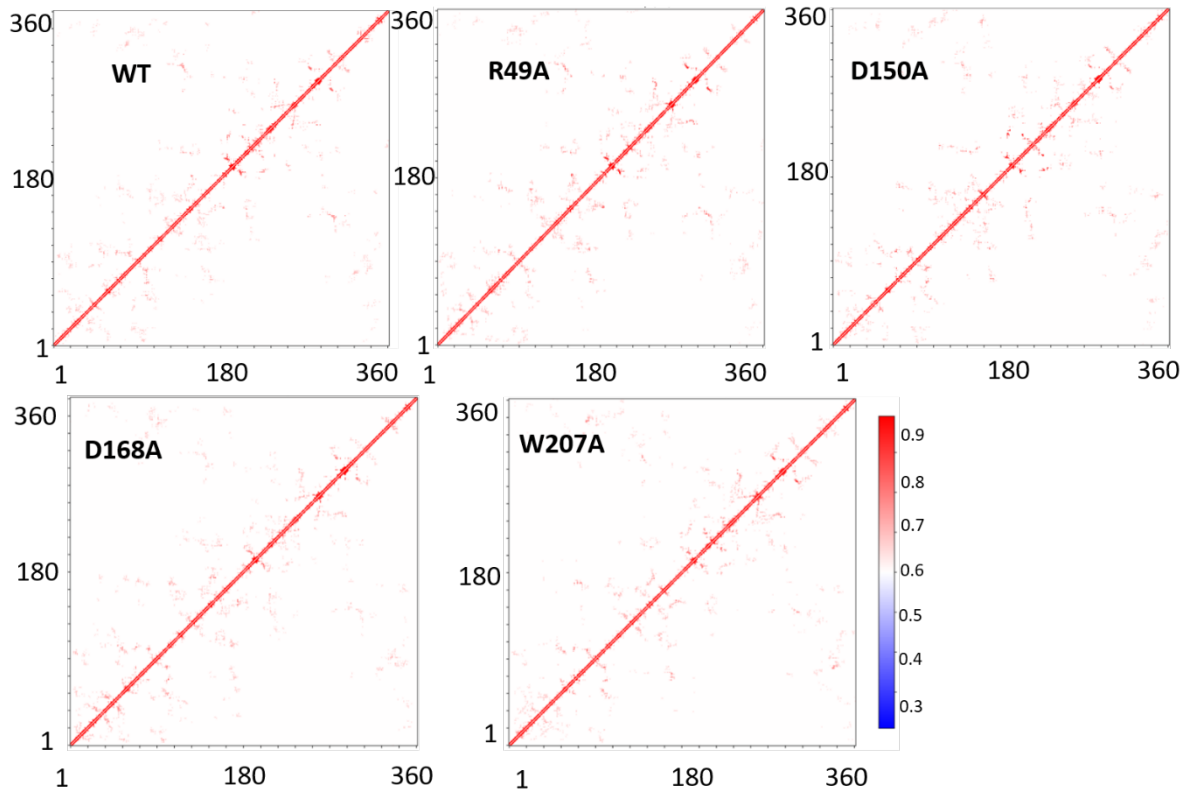

Fig. S8: Total correlation map of the WT and the mutants, obtained as generalised correlation coefficients through mutual information.

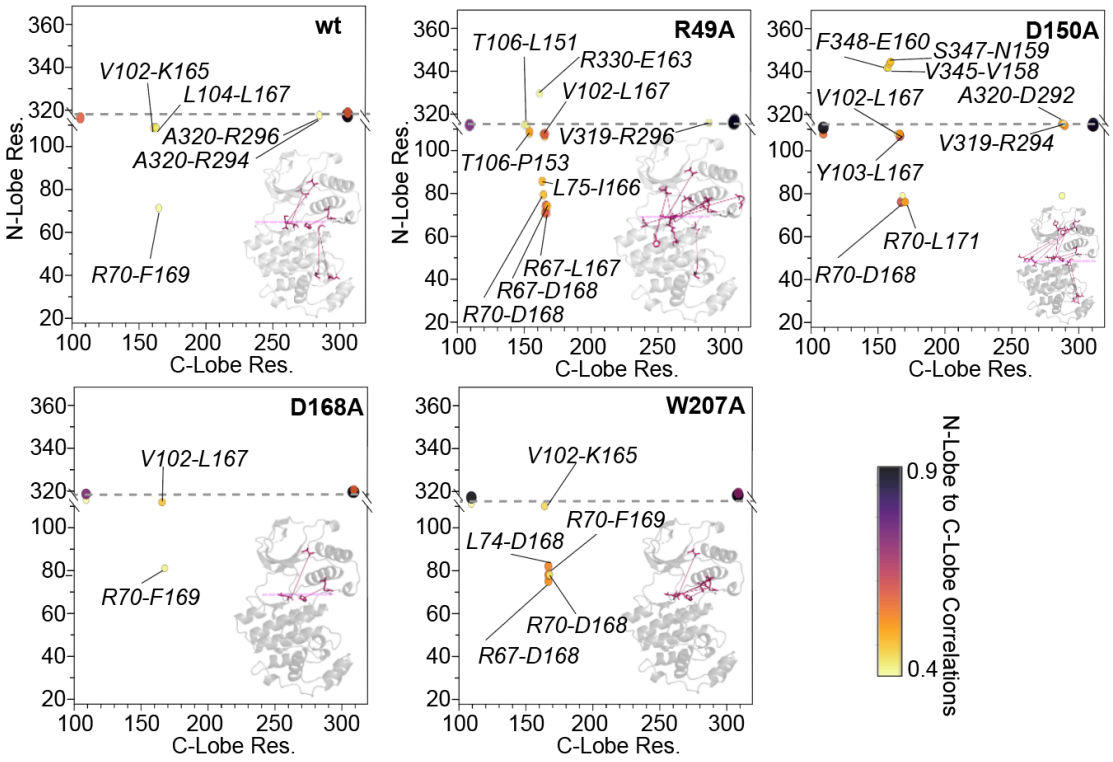

Fig. S9: N-C lobe correlations of the mutants using the correlation plots shown in Fig. S8 but focusing on the inter-domain regions. The correlation pairs are stated below in Table S3.

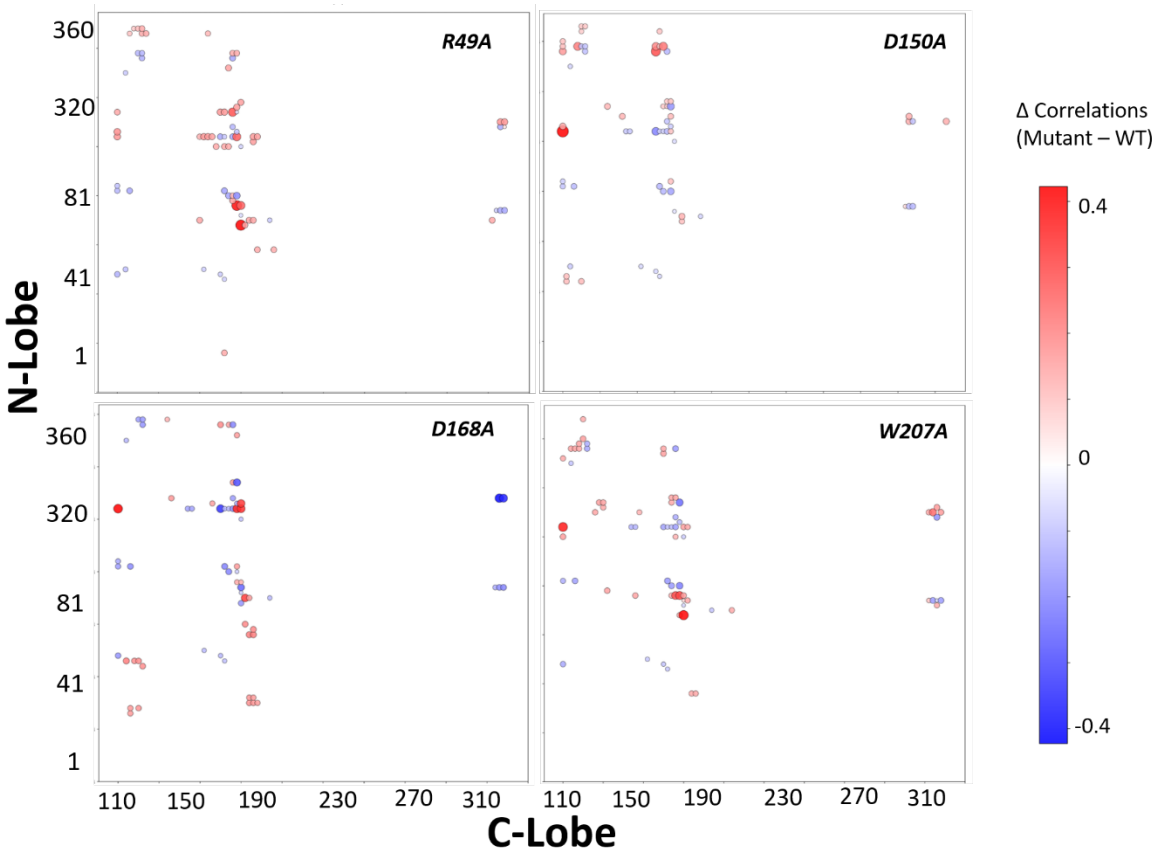

Fig. S10: Differences (mutant – WT) in the correlations from the N to C lobe for each of the mutants.

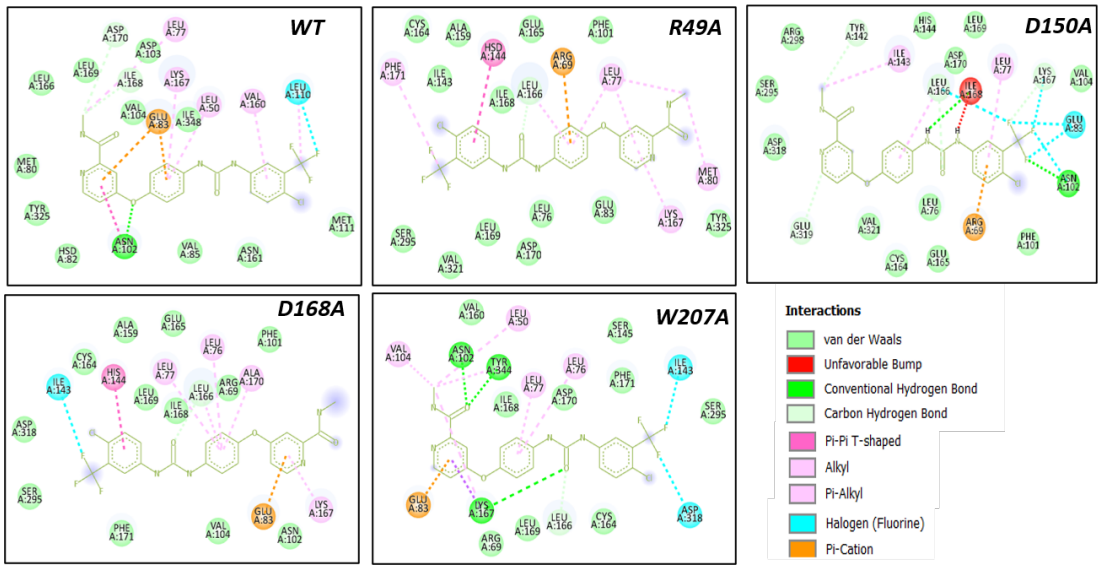

Fig. S11: Interacting residues when ligand sorafenib is docked with the WT protein and the mutants as seen through Discovery studio[13]. Note that the numbering of interacting residues provided by Discovery studio in this figure is shifted by +2 from the normal convention.

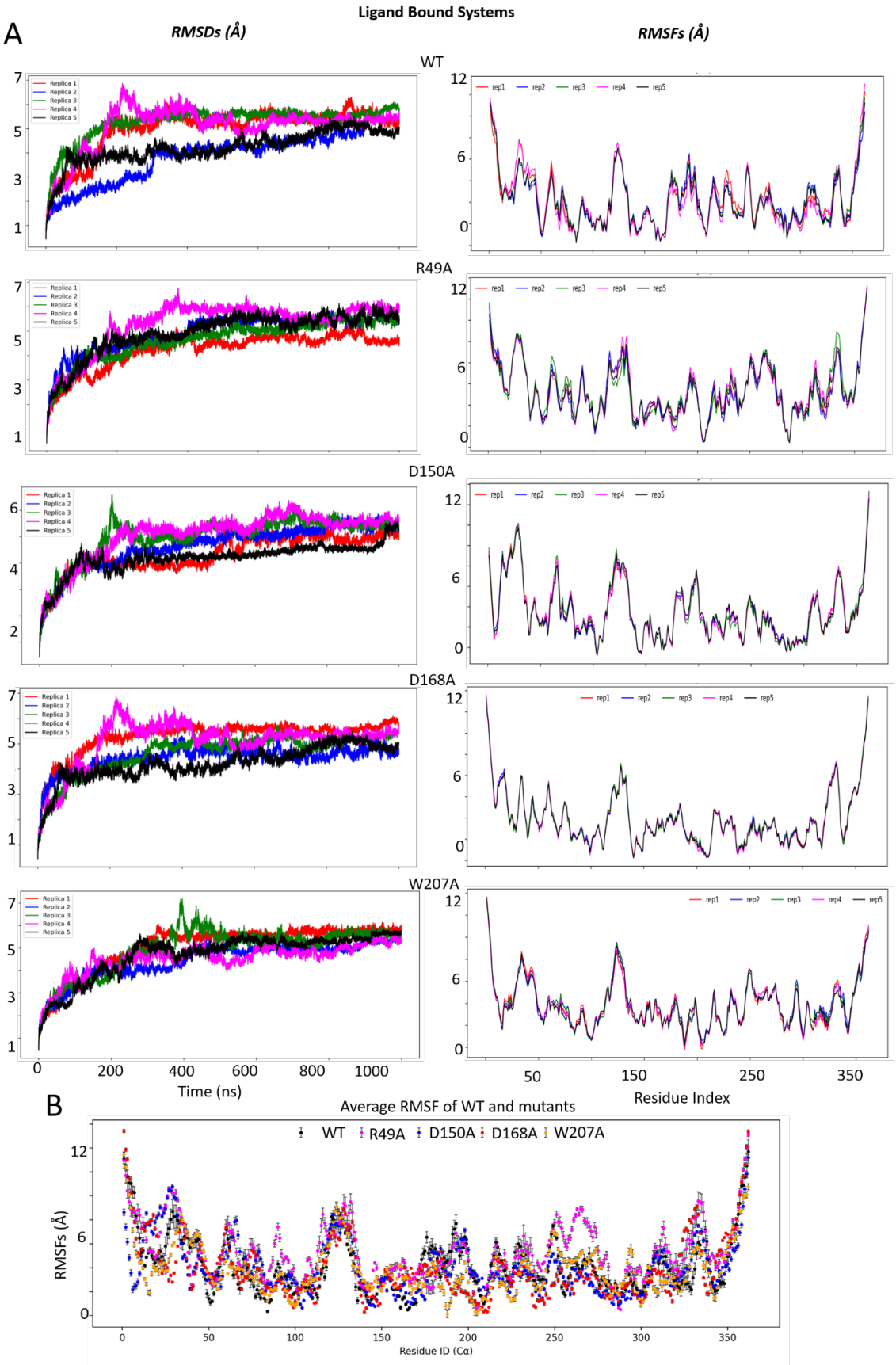

Fig. S12: A) RMSDs and RMSFs of five replicas per ligand-bound mutant. The last 200 ns each were used for network and correlation analysis. **B)** Mean and standard deviation of the RMSFs of the ligand-bound ensembles compared to each other.

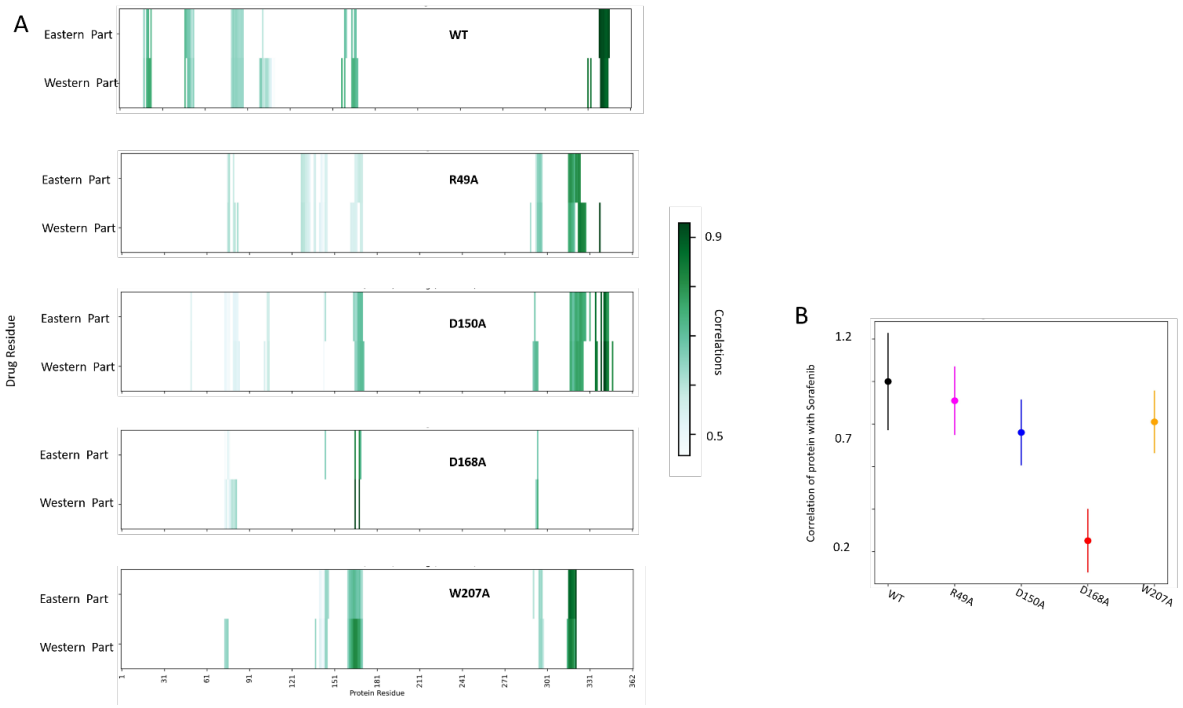

Fig. S13: Correlations of the ligand with the entire protein for WT and mutants. **A)** Relative correlations between the protein and the ligand (divided into two groups, the eastern and western part), resolved by protein residue. **B)** Total correlation of the ligand sorafenib with the mutants and the WT (the latter being normalized to 1).

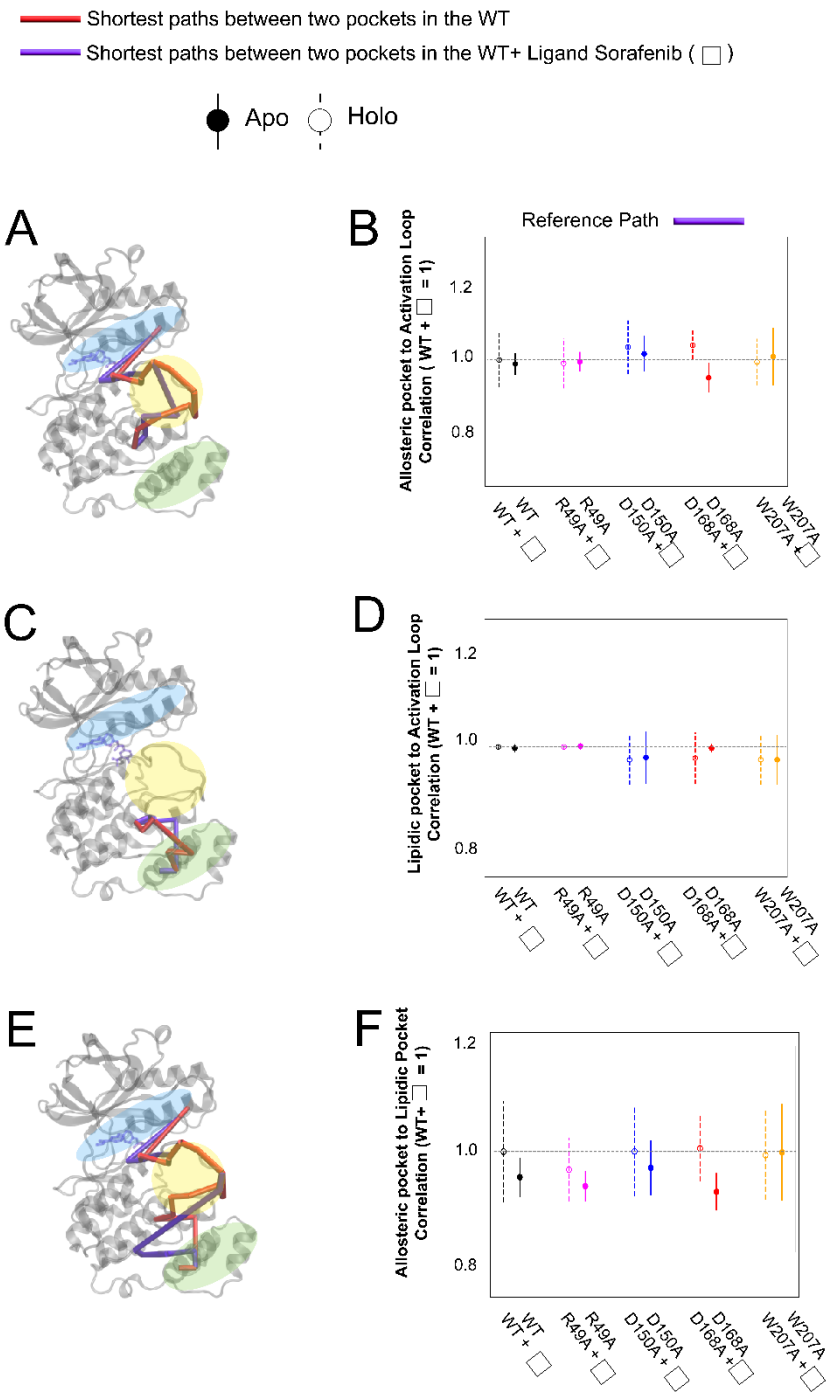

Fig S14: A) Structural depiction of the communication pathway from the allosteric pocket to the activation loop in wild-type p38α kinase. The apo WT shortest path is shown in red, while the ligand-bound (holo) WT pathway is depicted in purple, highlighting a shift in the nature of inter-residue motional interactions upon ligand binding. **B)** Correlational changes referenced to the holo WT pathway (purple). **C)** Structure of the lipid-pocket-to-activation-loop pathway, comparing apo (red) and holo (purple) WT forms. Ligand binding again alters the trajectory of this communication path. **D)** Using the holo WT pathway (purple) as the reference, minor differences in correlations are seen from the lipid pocket to the activation loop. **E)** Structural comparison of the allosteric-to-lipid pocket pathway, red and purple representing shortest paths in apo WT and holo WT, respectively. **F)** Correlation changes for the allosteric-site-to-lipid-pocket pathway.

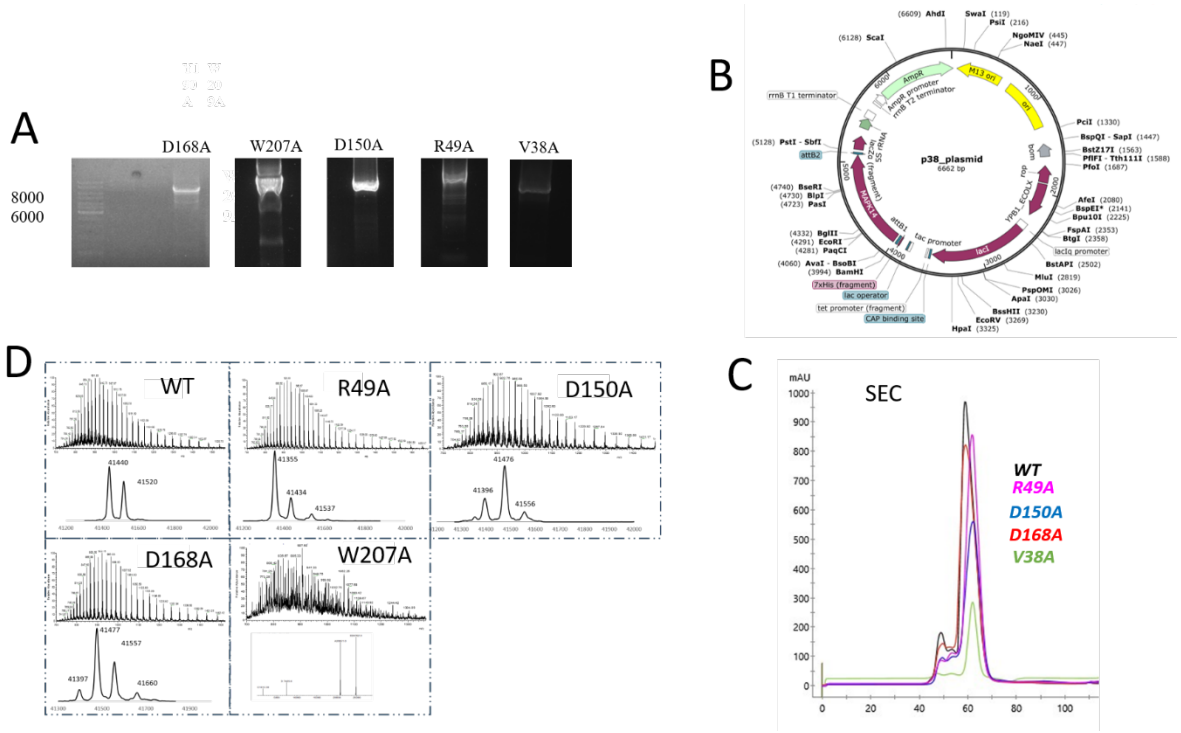

Fig. S15: **A**) Mutant DNA as seen through agarose gel electrophoresis. **B**) Plasmid of the entire p38α obtained through nanopore sequencing. **C**) Mass spectrometry results of the mutants and the WT, W209A shows a mix of different species. **D**) SEC of the pure triple labelled (DCN) protein (WT and the mutants).

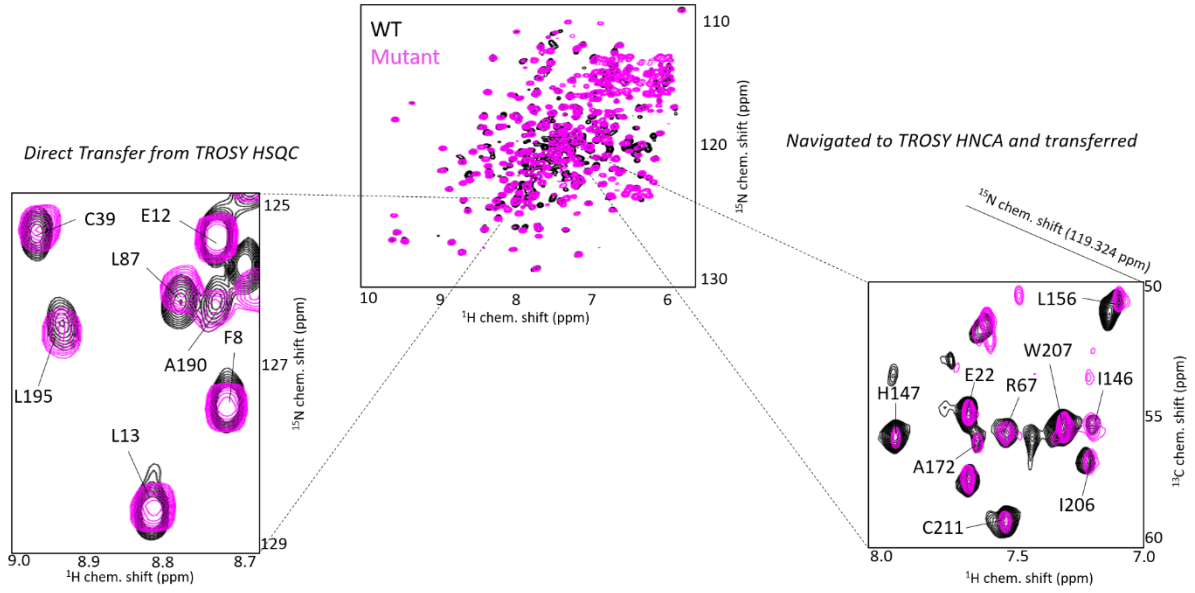

Fig. S16: Transfer of assignments using TROSY HSQC and HNCA spectra of the WT. (Chemical shifts of the WT are also available in the BMRB under accession code 17471.)

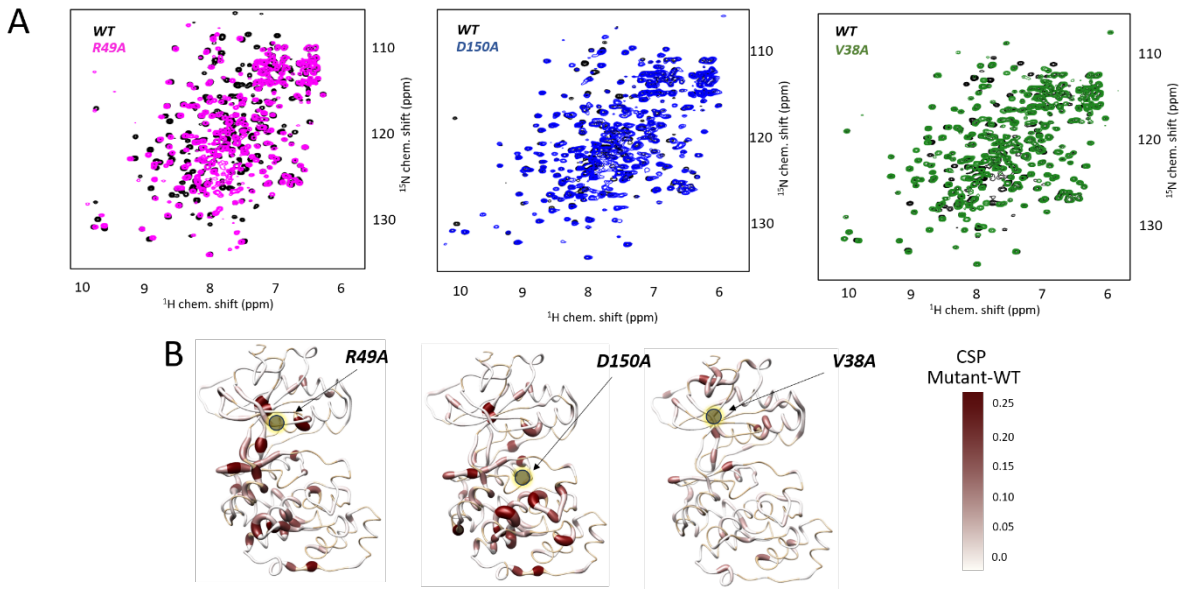

Fig. S17: A) TROSY-HSQC overlay of the mutants R49A, D150A, and negative control V38A with the WT. **B**) Structural representation of the chemical-shift perturbations.

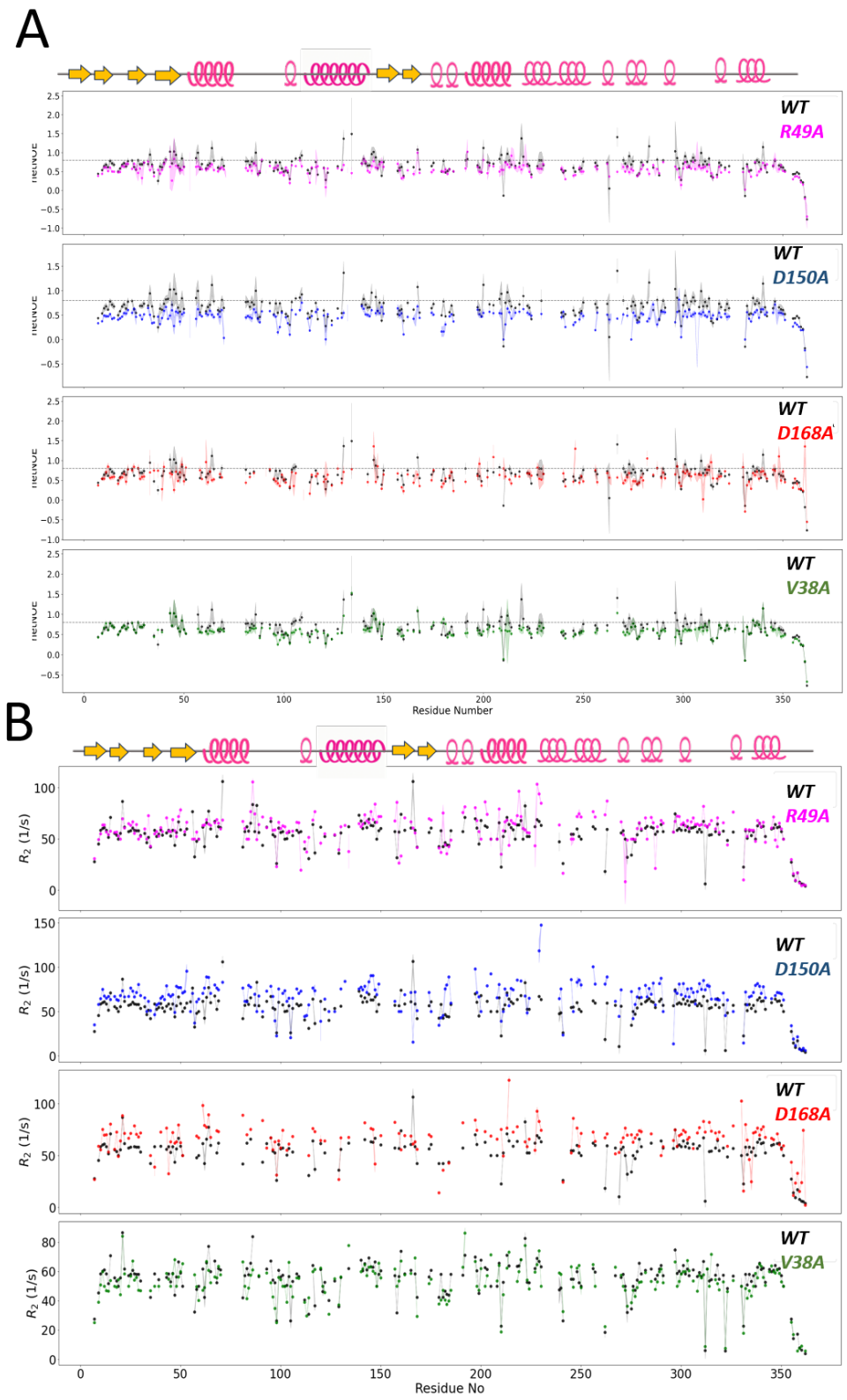

Fig. S18: A) Residue-wise hetNOE representation and comparison of the values (WT vs. mutants), including the negative control V38A. **B)** Residue-wise R_2 representation and comparison of the values (WT vs. mutants), including the negative control V38A.

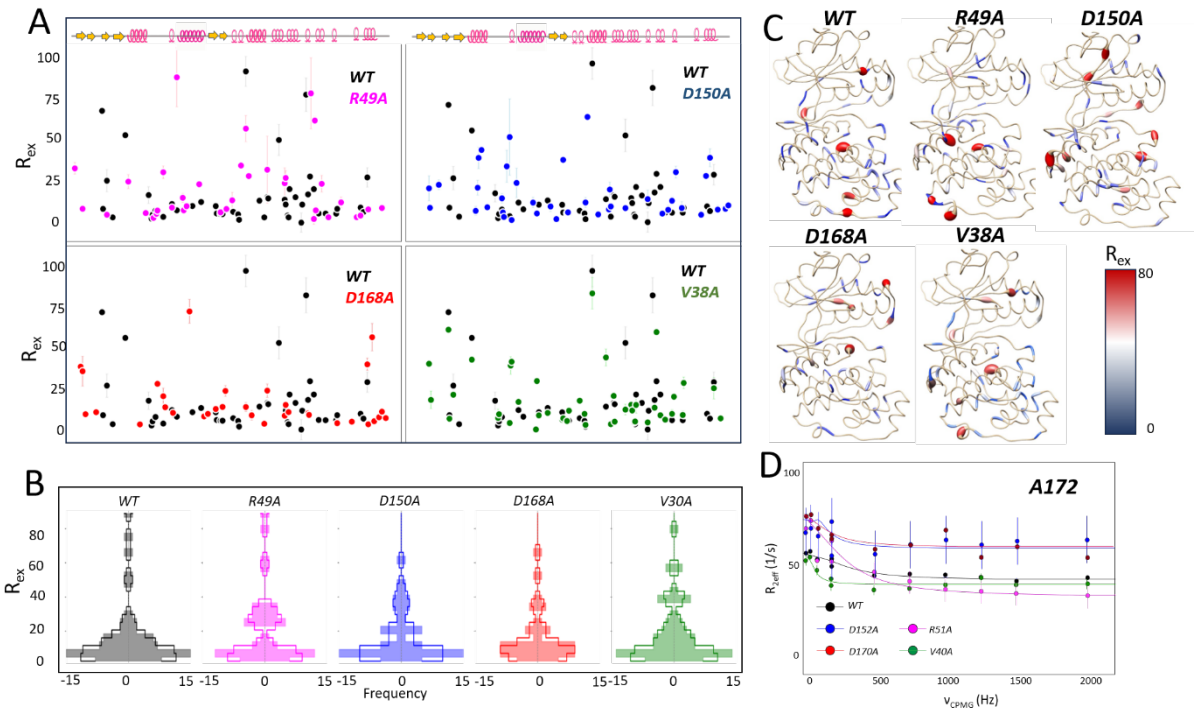

Fig. S19: A) Residue-wise comparison of ms timescale exchange contributions (R_{ex}) derived from CPMG relaxation dispersion experiments for wild-type and mutant variants (R49A, D150A, D168A, and V38A). Black denotes WT values; colored traces represent respective mutants. Mutants within the predicted dynamic network exhibit rather sporadic shifts in the location and magnitude of exchange-active residues. **B**) Histogram plots illustrating the global frequency distribution of R_{ex} values across all variants. The wildtype shows a slightly broader distribution of dynamic residues, indicative of a more homogeneous conformational ensemble. In contrast, network-disrupting mutants (e.g., D168A, R49A) display slightly more exchange. The minor differences hint to any motional changes rather being on timescales faster than the ms regime. **C)** Structural visualization comparing the spatial distribution of R_{ex} values between wild-type and the mutants. Residues exhibiting exchange contributions are highlighted in red. In panels A) to C), V38A shows minimal deviation from WT, consistent with its dynamic neutrality. **D**) Representative CPMG dispersion curves, shown here for residue A172, a key linker residue bridging the active site to the DFG motif.

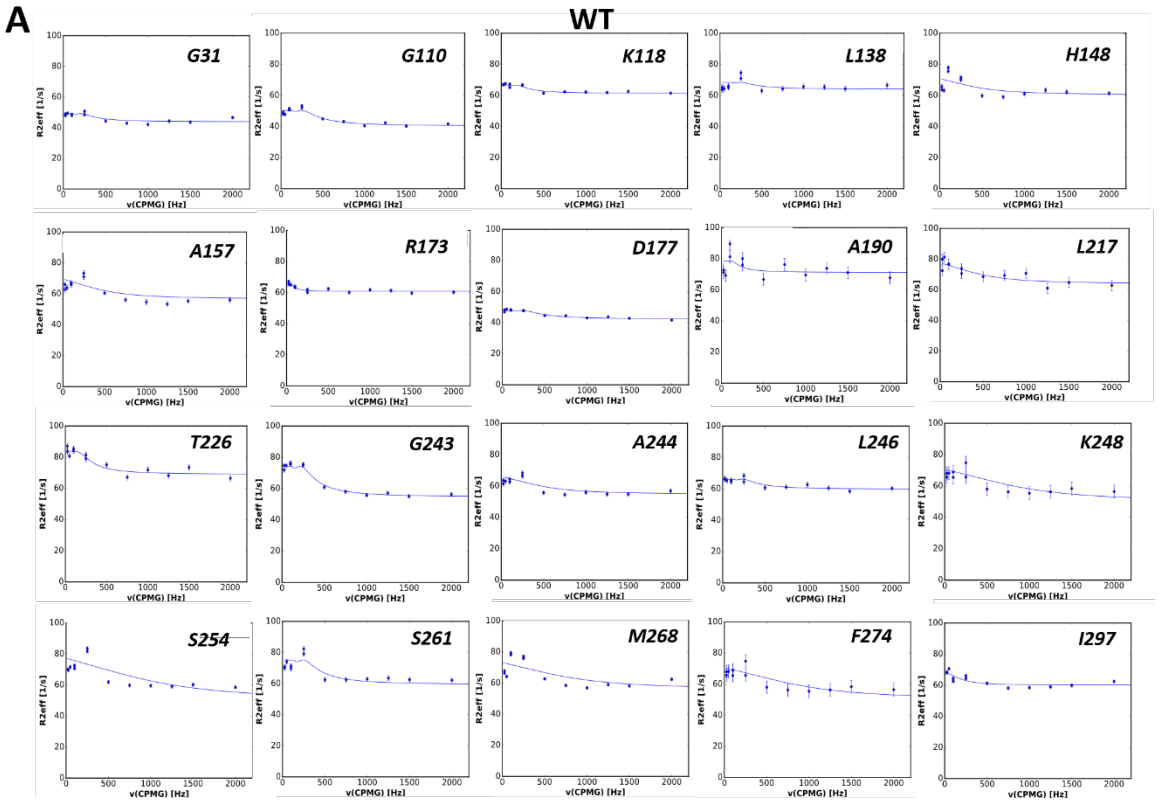
A
WT
G31
G110
K118
L138
H148
A157
R173
D177
A190
L217
T226
G243
A244
L246
K248
S254
S261
M268
F274
I297
R2eff [1/s]
v(CPMG) [Hz]

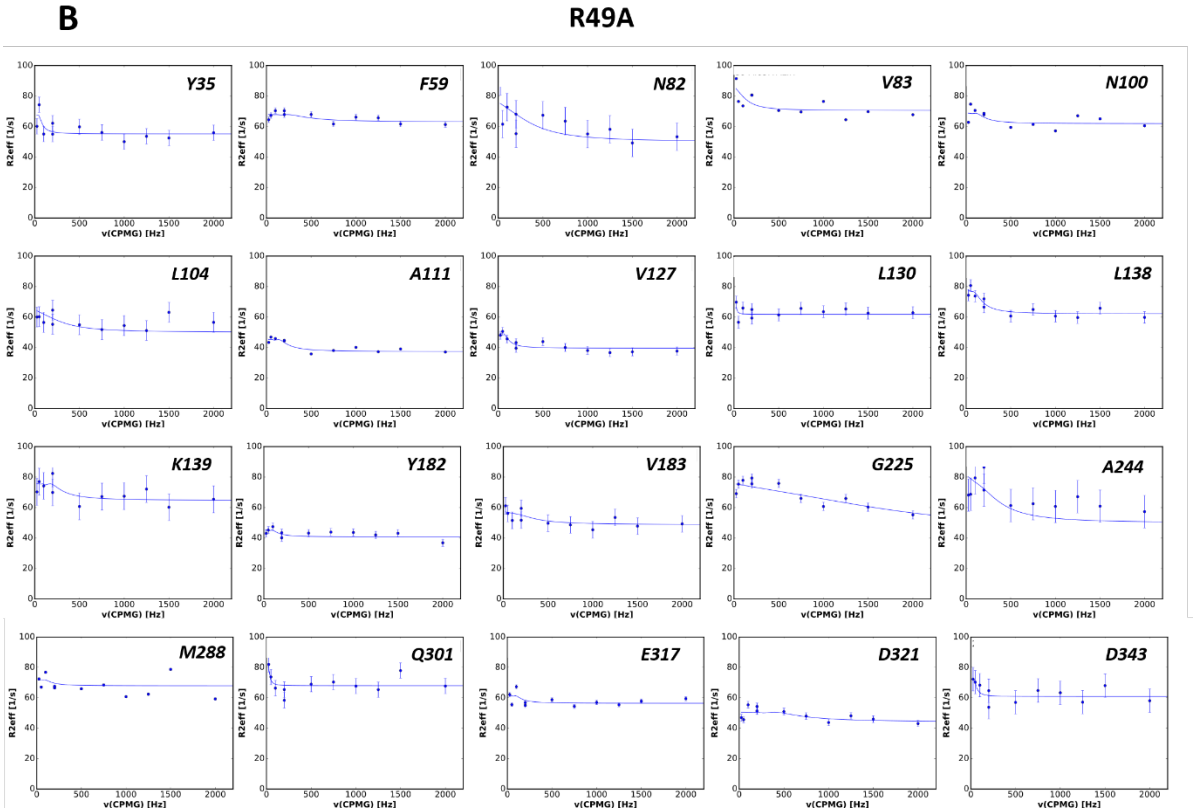
B
R49A
Y35
F59
N82
V83
N100
L104
A111
V127
L130
L138
K139
Y182
V183
G225
A244
M288
Q301
E317
D321
D343
R2eff [1/s]
v(CPMG) [Hz]

C **D150A**

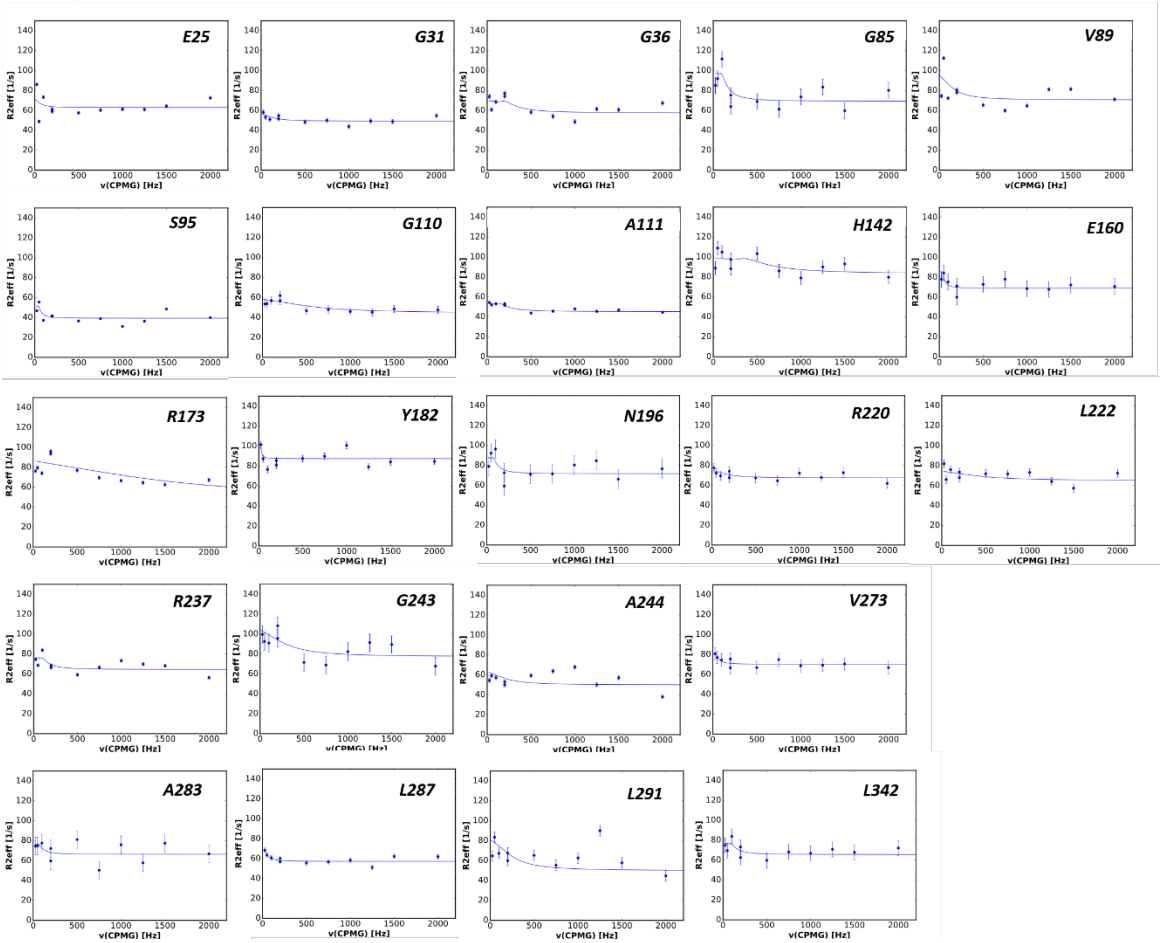

D **D168A**

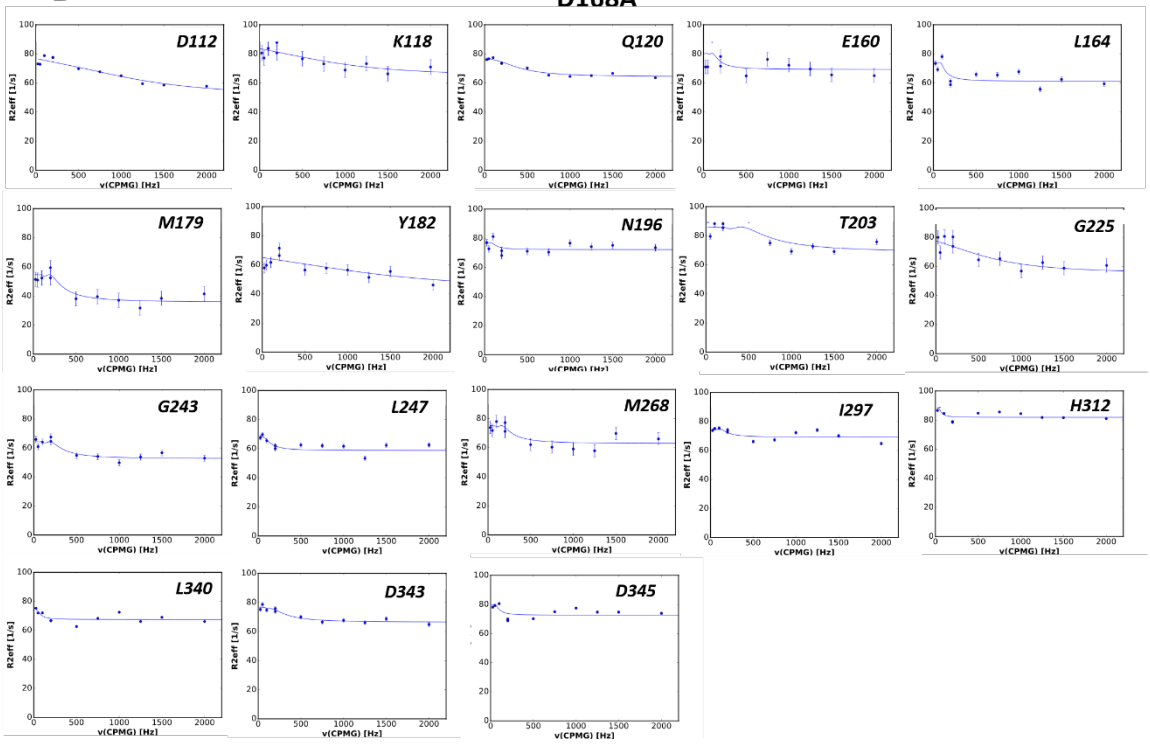

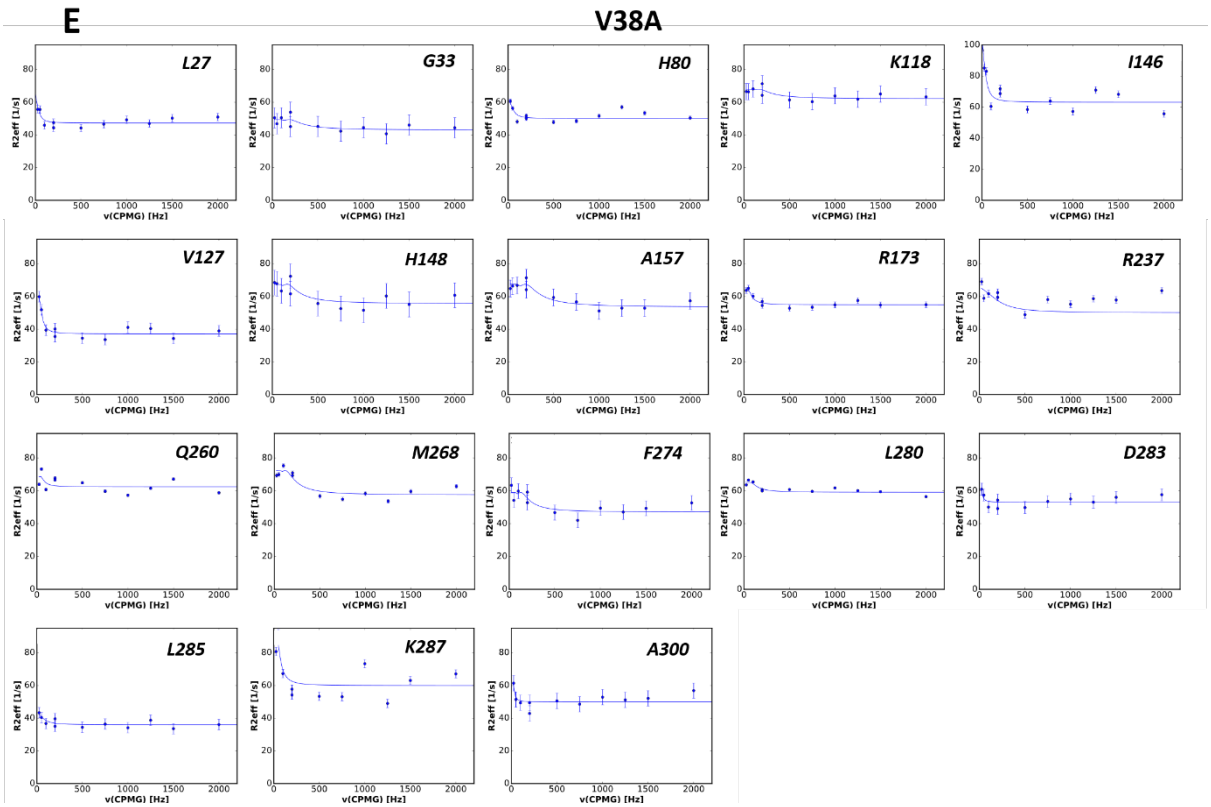

Fig. S20: A) CPMG curves of some residues for the WT. **B)** CPMG curves of some residues of the R49A protein. **C)** CPMG curves of some residues from D150A. **D)** CPMG curves of some residues from D168A. **E)** CPMG curves of some residues in V38A.

Supplementary tables

Table S1: Summary of Molecular Dynamics system parameters.

System	**Box** (Å)	**Total No. of Atoms**	**Salt Pairs (NaCl)**	**Salt Concentration** (M)	**No. of Water Molecules**
Wildtype apo	63.65 * 100.91* 84.81	66,679	56	0.151	19,896
R49A apo	79.60* 102.97 * 81.84	68,577	58	0.146	20,883
D150A apo	79.59 * 102.97* 81.84	68,593	59	0.146	20,885
D168A apo	79.85 * 102.87 * 81.35	68,566	59	0.147	20,678
W207A apo	79.61* 102.99 * 81.85	68,576	59	0.146	20,883
Wildtype holo	106.46 * 70.03 * 90.98	69,469	60	0.147	21,159
R49A holo	102.93 * 85.05 * 71.93	64,445	55	0.145	19,492
D150A holo	101.80 * 84.49 * 71.93	63,037	54	0.145	19,020

D168A holo	100.66 * 85.60 * 71.41	62,995	54	0.146	19,006
W207A holo	102.50 * 85.11 * 72.13	64,201	55	0.145	19,411
3HEG (crystal structure with Sorafenib)	96.32 * 76.65 * 67.13	50,932	42	0.140	14,979
3GCS (crystal structure with Sorafenib and β-OG)	94.64 * 68.08 * 74.74	49,421	41	0.141	14,489

Table S2: Residues showing highest betweenness centrality for the wildtype and mutants (with decreasing values from top to bottom in each of the columns).

WT	**R49A**	**D150A**	**D168A**	**W207A**
W207, I212	L135, N155	K165, D343	I131, D343	R14, I52
R136, I141	R149, T185	V105, L156	I131, L135	E141, L166
R136, T203	N155, N159	D205, S208	G210, L236	L205, V236
D150, D168	N14, E160	S154, R173	L135, G210	R139, E141
P29, R49	V117, I134	S154, S208	V102, I142	R135, M165
R136, W207	N14, N159	Y140, M288	I134, G137	I52, E66
K66, I141	I116, V158	K338, D343	N100, V102	E141, T167
W205, I210	I134, G137	H142, L280	G47, V102	G145, G170
Y140, D205	K66, K165	H142, L156	L236, S254	E274, T293
Y188, T203	G137, V273	H80, C162	C39, G47	E48, I102

Table S3: Correlation Values Between N-lobe to C-Lobe.

WT			**R49A**			**D150A**			**D168A**			**W207A**		
N-lobe res.	C-lobe res.	Corr. val.	N-lobe res.	C-lobe res.	Corr. val.	N-lobe res.	C-lobe res.	Corr. val.	N-lobe res.	C-lobe res.	Corr. val.	N-lobe res.	C-lobe res.	Corr. val.
319	316	0.96	319	316	0.96	319	316	0.96	317	316	0.96	317	316	0.95
319	315	0.75	319	315	0.94	106	108	0.95	317	315	0.93	106	108	0.94
106	108	0.55	320	316	0.93	320	316	0.91	106	108	0.75	317	315	0.93
320	316	0.55	106	108	0.76	319	315	0.75	318	316	0.55	318	316	0.72
102	165	0.36	70	168	0.58	102	167	0.61	102	167	0.41	70	168	0.53
102	167	0.35	102	167	0.57	70	168	0.59	70	169	0.35	74	168	0.52
70	169	0.31	67	168	0.57	103	108	0.54	103	108	0.32	67	168	0.51
319	294	0.31	103	155	0.46	319	294	0.48	317	316	0.96	102	165	0.40

319	316	0.96	70	169	0.43	70	171	0.46	317	315	0.93	70	169	0.38
319	315	0.75	81	165	0.42	103	167	0.46	106	108	0.75	103	108	0.35
106	108	0.55	101	167	0.41	320	292	0.46	318	316	0.55	317	316	0.95
320	316	0.55	102	166	0.41	348	160	0.40	102	167	0.41	106	108	0.94
102	165	0.36	67	167	0.41	347	159	0.39	70	169	0.35	317	315	0.93
102	167	0.35	75	166	0.41	345	158	0.37	103	108	0.32	318	316	0.72
70	169	0.31	319	296	0.33	345	157	0.35				70	168	0.53
319	294	0.31	106	153	0.32	318	293	0.31				74	168	0.52
			106	151	0.32	73	292	0.31				67	168	0.51
			330	163	0.31	73	169	0.30				102	165	0.40
			102	155	0.31	70	170	0.30				70	169	0.38
			319	316	0.96	103	165	0.30				103	108	0.35
			319	315	0.94	319	316	0.96						
			320	316	0.93	106	108	0.95						
			106	108	0.76	320	316	0.91						
			70	168	0.58	319	315	0.75						
			102	167	0.57	102	167	0.61						
			67	168	0.57	70	168	0.59						
			103	155	0.46	103	108	0.54						
			70	169	0.43	319	294	0.48						
			81	165	0.42	70	171	0.46						
						103	167	0.46						

Table S4: B-factors of key network residues, derived from PDB 3HEG.

Residue	**B-factor** (Å^2)
PRO29	0.434
ARG49	0.509
LYS66	0.206
ILE141	0.199
ASP150	0.342
ASP168	0.497
TYR188	0.111
THR203	0.207
TRP207	0.056
ILE212	0.107
ILE235	0.098

Table S5: Pathways to and from different pockets.

Apo Pathway (red)	Allosteric Pocket to Activation Loop	{ K66 R67 } { R67 L167 } { L167 D168 } { D168 G170 } { G170 A172 } { A172 R173 } { R173 T175 } { T175 Y182 } { Y182 V183 } { V183 A184 } { A184 Y188 }
	Lipid Pocket to Activation Loop	{ R186 W187 } { W187 Y188 } { Y188 R189 } { R189 D227 } { D227 I229 } { I229 Q231 } { Q231 K233 } { K233 I235}
	Allosteric Pocket to lipid Pocket	{ K66 R67 } { R67 L167 } { L167 D168 } { D168 G170 } { G170 A172 } { A172 R173 } { R173 T175 } { T175 A176 } { A176 G178 } { G178 M179 } { M179 T221 } { T221 L222 } { L222 P224 } { P224 L232 } { L232 I235 }
Holo Pathway (purple)	Allosteric Pocket to Activation Loop	{ K66 D168 } { D168 F169 } { F169 L171 } { L171 R173 } { R173 T175 } { T175 A176 } { A176 G178 } { G178 T180 } { T180 G181 } { G181 V183 } { V183 T185 } { T185 Y188 }
	Lipid Pocket to Activation Loop	{ Y188 R189 } { R189 Y188 } { Y188 T221 } { T221 K233 } { K233 I235 }
	Allosteric Pocket to lipid Pocket	{ K66 D168 } { D168 F169 }

		{ F169 L171 } { L171 R173 } { R173 T175 } { T175 A176 } { A176 G178 } { G178 T180 } { T180 G181 } { G181 V183 } { V183 A184 } { A184 R186 } { R186 Y188 } { Y188 T221 } { T221 K233 } { K233 I235 }

Table S6 : p-values for shortest-path analysis.

Reference	Path	Comparison	Bootstrap p-value
Apo WT (Red)	Allosteric – Activation	WT vs 51	0.1862
		WT vs 152	0.1664
		WT vs 170	0.1414
		WT vs 209	0.0394 **
		WT vs LWT	0.0382 **
		WT vs L51	0.1131
		WT vs L152	0.2539
		WT vs L170	0.3698
		WT vs L209	0.8573
	Lipid – Activation	WT vs 51	0.0761
		WT vs 152	0.1582
		WT vs 170	0.0425 **
		WT vs 209	0.1273
		WT vs LWT	0.3124
		WT vs L51	0.2878
		WT vs L152	0.3923
		WT vs L170	0.7980
		WT vs L209	0.6744
	Allosteric – Lipid	WT vs 51	0.0171 **
		WT vs 152	0.0026 **
		WT vs 170	0.0022 **
		WT vs 209	0.0005 ***
		WT vs LWT	0.0779
		WT vs L51	0.0017 **
		WT vs L152	0.0034 **
		WT vs L170	0.0023 **
		WT vs L209	0.0145 **
Holo WT (Purple)	Allosteric – Activation	LWT vs WT	0.7758
		LWT vs 51	0.9056
		LWT vs 152	0.6795
		LWT vs 170	0.2472
		LWT vs 209	0.8481

		LWT vs L51	0.8465
		LWT vs L152	0.4681
		LWT vs L170	0.3202
		LWT vs L209	0.9079
	Lipid – Activation	LWT vs WT	0.5132
		LWT vs 51	0.6847
		LWT vs 152	0.4070
		LWT vs 170	0.5226
		LWT vs 209	0.3013
		LWT vs L51	0.99998
		LWT vs L152	0.3079
		LWT vs L170	0.3925
		LWT vs L209	0.3135
	Allosteric – Lipid	LWT vs WT	0.3397
		LWT vs 51	0.2093
		LWT vs 152	0.5540
		LWT vs 170	0.1568
		LWT vs 209	0.9789
		LWT vs L51	0.5246
		LWT vs L152	0.9953
		LWT vs L170	0.9076
		LWT vs L209	0.9113

Table S7: K_M, v_{max} and EC values. Note that v_{max} (needs to be read as relative values as the conversion between fluorescence and concentrations is unknown) is not reliable as the protein concentrations and degree of phosphorylation might be slightly different between samples.

Protein	**WT**	**D168A**	**R49A**	**D150A**	**W207A**	
K_M (μM)	2.4+/-0.7	3.9+/-0.1	3.7+/-0.2	3.3+/-0.1	2.6+/-0.1	*from ATP plot*
v_{max} (a.u.)	5.2+/-0.2	4.3+/-0.7	3.3+/-0.8	1.3+/-0.3	1.6+/-0.4	
R-sq	0.93	0.97	0.96	0.94	0.94	
K_M (nM)	56.34 ± 5.0	95.89 ± 4.7	116.24 ± 5.9	95.82 ± 6.5	88.44 ± 11.7	*from substrate plot*
r^2	0.99	0.99	0.99	0.99	0.99	

Table S8: Docking results of WT and mutant with Sorafenib at the allosteric pocket (in kcal/mol).

WT	**R49A**	**D150A**	**D168A**	**W207A**
-8.74	-3.69	-3.58	-6.56	-3.20
-7.74	-2.70	-3.35	-6.01	-0.35
-7.14		-2.72	-5.67	-0.35
-6.08		-1.70		-0.30
				-0.25

References :

(1) Phillips, J. C.; Hardy, D. J.; Maia, J. D. C.; Stone, J. E.; Ribeiro, J. V.; Bernardi, R. C.; Buch, R.; Fiorin, G.; Hénin, J.; Jiang, W.; et al. Scalable molecular dynamics on CPU and GPU architectures with NAMD. *J. Chem. Phys.* **2020**, *153* (4), 044130. DOI: 10.1063/5.0014475

(2) Ribeiro, J. V.; Bernardi, R. C.; Rudack, T.; Stone, J. E.; Phillips, J. C.; Freddolino, P. L.; Schulten, K. QwikMD - Integrative Molecular Dynamics Toolkit for Novices and Experts. *Sci. Rep.* **2016**, *6*, 26536. DOI: 10.1038/srep26536

(3) Namboodiri, H. V.; Bukhtiyarova, M.; Ramcharan, J.; Karpusas, M.; Lee, Y.; Springman, E. B. Analysis of imatinib and sorafenib binding to p38alpha compared with c-Abl and b-Raf provides structural insights for understanding the selectivity of inhibitors targeting the DFG-out form of protein kinases. *Biochemistry* **2010**, *49* (17), 3611-3618. DOI: 10.1021/bi100070r

(4) Simard, J. R.; Getlik, M.; Grütter, C.; Pawar, V.; Wulfert, S.; Rabiller, M.; Rauh, D. Development of a fluorescent-tagged kinase assay system for the detection and characterization of allosteric kinase inhibitors. *J. Am. Chem. Soc.* **2009**, *131* (37), 13286-13296. DOI: 10.1021/ja902010p

(5) Wilson, K. P.; Fitzgibbon, M. J.; Caron, P. R.; Griffith, J. P.; Chen, W.; McCaffrey, P. G.; Chambers, S. P.; Su, M. S. Crystal structure of p38 mitogen-activated protein kinase. *J. Biol. Chem.* **1996**, *271* (44), 27696-27700. DOI: 10.1074/jbc.271.44.27696

(6) Melo, M. C. R.; Bernardi, R. C.; de la Fuente-Nunez, C.; Luthey-Schulten, Z. Generalized correlation-based dynamical network analysis: a new high-performance approach for identifying allosteric communications in molecular dynamics trajectories. *J. Chem. Phys.* **2020**, *153* (13), 134104. DOI: 10.1063/5.0018980

(7) Michaud-Agrawal, N.; Denning, E. J.; Woolf, T. B.; Beckstein, O. MDAnalysis: a toolkit for the analysis of molecular dynamics simulations. *J. Comput. Chem.* **2011**, *32* (10), 2319-2327. DOI: 10.1002/jcc.21787

(8) Lam, S. K.; Pitrou, A.; Seibert, S. Numba: a LLVM-based Python JIT compiler. In Proceedings of the Second Workshop on the LLVM Compiler Infrastructure in HPC, Austin, Texas; 2015.

(9) Behnel, S.; Bradshaw, R.; Citro, C.; Dalcin, L.; Seljebotn, D. S.; Smith, K. Cython: The Best of Both Worlds. *Comput. Sci. Eng.* **2011**, *13* (2), 31-39. DOI: 10.1109/MCSE.2010.118.

(10) William, H.; Andrew, D.; Klaus, S. VMD: Visual molecular dynamics. *J. Mol. Graph.* **1996**, *14* (1), 33-38. DOI: https://doi.org/10.1016/0263-7855(96)00018-5.

(11) Skinner, S. P.; Fogh, R. H.; Boucher, W.; Ragan, T. J.; Mureddu, L. G.; Vuister, G. W. CcpNmr AnalysisAssign: a flexible platform for integrated NMR analysis. *J. Biomol. NMR* **2016**, *66* (2), 111-124. DOI: 10.1007/s10858-016-0060-y

(12) Bieri, M.; Gooley, P. R. Automated NMR relaxation dispersion data analysis using NESSY. *BMC Bioinformatics* **2011**, *12*, 421. DOI: 10.1186/1471-2105-12-421

(13) Haque, A.; Baig, G. A.; Alshawli, A. S.; Sait, K. H. W.; Hafeez, B. B.; Tripathi, M. K.; Alghamdi, B. S.; Mohammed Ali, H. S. H.; Rasool, M. Interaction Analysis of MRP1 with Anticancer Drugs Used in Ovarian Cancer: In Silico Approach. *Life* **2022**, *12* (3), 383.